RSC Advances

PAPER

View Article Online
View Journal | View Issue

Cite this: *RSC Adv.*, 2025, **15**, 34068

Room-temperature synthesis of silver-based nanoparticle-embedded hydrogel material *via* catalytic crosslinking for recyclable dye degradation applications

Damini Jagankar,[a] Nikita Das,[a] Amitava Mukherjee [b] and Chandan Maity *[a]

A simple, one-pot, facile room-temperature synthesis method is developed for the fabrication of silver-based nanoparticles embedded within a hydrazone-based hydrogel matrix. The hydrogel matrix is prepared under ambient conditions *via* acid catalysis by mixing aqueous solutions of the molecular building blocks. The hydrogel network serves as a template for the *in situ* formation of silver-oxide nanoparticles (Ag_2O NPs) enabling their uniform dispersion and stabilization within the matrix. Ag_2O NPs can subsequently be converted to silver nanoparticles (Ag NPs) by treating them with an aqueous solution of sodium borohydride ($NaBH_4$). The resulting composite material exhibits rapid catalytic degradation of Congo red (CR) and methyl orange (MO), achieving over 95% degradation efficiency within 5 minutes under ambient conditions in both individual and mixed dye systems. Furthermore, the composite effectively degrades real textile industry wastewater samples. The material also demonstrates excellent reusability, retaining its catalytic performance over multiple cycles without significant loss of activity. These findings demonstrate the potential of *in situ* synthesized nanoparticle-embedded hydrogel systems as efficient, recyclable, and environmentally friendly platforms for the catalytic degradation of organic dyes.

Received 22nd May 2025
Accepted 11th September 2025

DOI: 10.1039/d5ra03595c

rsc.li/rsc-advances

Introduction

Sustainable strategies for mitigating environmental pollution require the development of advanced functional materials capable of efficiently removing harmful contaminants. Materials that can be synthesized under ambient conditions, without the need for high temperatures or complex procedures, offer significant advantages in terms of cost-effectiveness and practical applicability, particularly in resource-limited settings. In this context, hydrogel networks embedded with nanoparticles (NPs) represent a promising platform for engineering composite materials with enhanced functional properties.[1–6] Due to their unique physicochemical characteristics, such materials are well-suited for a variety of applications, including catalysis,[7] biosensing,[8] drug delivery,[9] and environmental remediation.[10] In recent years, a variety of composite systems have been developed by incorporating different classes of NPs such as metals, metal oxides, non-metals, and polymeric moieties into polymeric/supramolecular hydrogel matrices.[11] Among these, silver (Ag)-based nanoparticle-embedded hydrogels have gained particular attention owing to their multifunctionality and wide-ranging applications across materials science, environmental engineering, and biomedical fields.[12–14] However, the unique properties of Ag-based NPs are highly dependent on their nanoscopic dimensions. Therefore, precise control over particle size is critical for their effective application.[15] One promising strategy to achieve this involves the *in situ* synthesis of Ag-based NPs within molecular network architectures such as biological macromolecules, synthetic polymers, microgels, or hydrogels, which enables the formation of well-defined nanoparticle morphologies.[16–19] Among these, three-dimensional (3D) hydrogel networks offer distinct advantages over conventional non-aqueous or purely polymeric systems. The porous structure of hydrogels provides confined spaces that can function as nanoreactors, facilitating the nucleation and controlled growth of nanocrystals.[20,21]

Hydrogels derived from natural biomaterials such as alginate, lignin, chitosan, and carboxymethylcellulose are particularly attractive due to their abundance, low cost, easy accessibility, and environmental sustainability.[22–24] Among these biopolymers, alginate is particularly promising due to its ability to form hydrogels under mild aqueous conditions, combined with excellent biocompatibility and tuneable physicochemical properties. These attributes make alginate-based

[a](Organic)Material Science and Engineering Laboratory, CNBT, Vellore Institute of Technology, Tamil Nadu-632014, India. E-mail: chandanmaitylab@gmail.com; chandan.maity@vit.ac.in

[b]Centre for Nanobiotechnology (CNBT), Vellore Institute of Technology, Tamil Nadu-632014, India

hydrogels especially suitable for applications in both biomedical and environmental fields.[25]

Conventional approaches for synthesizing Ag-based NPs, typically involving physical or chemical crosslinking, are often constrained by the use of toxic reducing agents and/or the requirement for harsh conditions such as elevated temperatures, high pressures, light irradiation, or specialized instrumentation.[26–30] These limitations highlight the need for greener and more sustainable synthetic methodologies. In this context, an environmentally friendly approach that enables the formation of a hydrogel network and the controlled synthesis of Ag-based NPs within the hydrogel matrix at room temperature, without the use of toxic chemicals, is highly desirable for environmental remediation applications.

Herein, we report a green, facile, and *in situ* synthesis method for Ag-based nanoparticles within an alginate-based hydrogel matrix (Alg-Hy, Fig. 1a). We demonstrate that both the formation of Alg-Hy and the resulting properties of the hydrogel matrix can be effectively controlled *via* acid catalysis under ambient conditions. The hydrogel network serves as a nanoconfined platform for the nucleation and growth of Ag-based NPs.

By simply mixing aqueous solutions of the precursor building blocks under ambient conditions, silver oxide nanoparticles (Ag_2O NPs) are formed *in situ* within the alginate-based hydrogel matrix (Ag_2O NPs/Alg-Hy, Fig. 1b). The hydrogel matrix stabilizes the Ag_2O NPs and prevents their aggregation. Notably, this synthesis does not require external reducing agents, elevated temperatures, or specialized instrumentation. Furthermore, the embedded Ag_2O NPs can be readily reduced to metallic silver nanoparticles (Ag NPs) within the hydrogel matrix upon treatment with an aqueous solution of sodium borohydride ($NaBH_4$). The resulting composite (Ag NPs/Alg-Hy, Fig. 1b) exhibits rapid catalytic activity, achieving over 95% degradation efficiency of Congo red (CR) and methyl orange (MO) in individual dye solutions, mixed dye systems, as well as textile dye-containing wastewater, all under ambient conditions. Moreover, the composite displays excellent recyclability, retaining high catalytic performance over multiple degradation cycles without significant loss of activity.

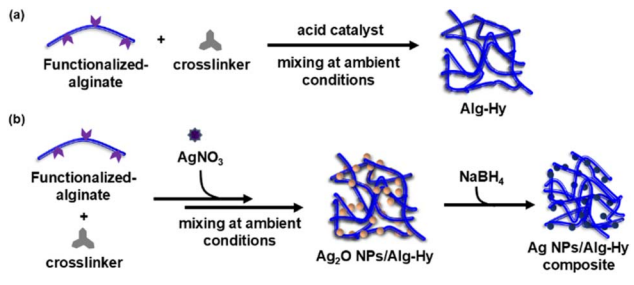

Fig. 1 Schematic illustration of the preparation of Ag NPs-integrated alginate hydrogel material: (a) *in situ* formation of the alginate hydrogel matrix (Alg-Hy) *via* acid-catalysed crosslinking, (b) incorporation of Ag_2O NPs into the Alg-Hy matrix by mixing precursor solutions under ambient conditions, followed by *in situ* reduction of Ag_2O NPs to Ag NPs using $NaBH_4$.

Overall, the Ag-based NPs/Alg-Hy system exemplifies the effective synergistic integration of catalytic nanoparticles within a hydrogel matrix for the efficient removal of dye pollutants. The development of such multifunctional and recyclable composite materials offers a promising and sustainable strategy for tackling complex environmental pollution challenges in a sustainable and scalable manner.

Experimental

Materials and methods

***In situ* preparation of Alg-Hy material.** The alginate-based hydrogel material was prepared by mixing aqueous solutions of the precursor components at room temperature. Briefly, aqueous solutions of Alg-A (10.0 mg for 1.0 wt%) and GH (7.0 mg, 50.0 mM) in phosphate buffer (0.1 M) were combined at room temperature. Gelation was assessed using the vial inversion method. To determine the minimum gelation concentration (MGC) of Alg-Hy, various concentrations of Alg-A (0.5 wt% and 1.0 wt%) were mixed with GH at different concentrations (27 mM, 28 mM, 30 mM, 40 mM, and 50 mM). The MGC for GH to form stable hydrogel material with Alg-A (1 wt%) at pH 5 was 28 mM, whereas it was 40 mM at pH = 7.

***In situ* preparation of Ag_2O NPs/Alg-Hy material.** The Ag_2O NPs/Alg-Hy composite was prepared under ambient conditions by mixing aqueous solutions of the precursor components. Specifically, aldehyde-functionalized alginate (1.0 wt% in 1.0 mL), GH (7.0 mg, 50.0 mM), and $AgNO_3$ (5.1 mg, 30.0 mM) were combined at room temperature. The resulting mixture was kept in the dark. Hydrogel formation was observed after 1 hour and confirmed using the vial inversion method. A pale-yellow coloration of the hydrogel developed within 2 hours, which remained unchanged over a 24 hour period. This characteristic pale-yellow color is indicative of the formation of Ag_2O NPs within the Alg-Hy matrix.

Catalytic degradation of organic dyes. The composite material was evaluated for its catalytic activity in the degradation of CR and MO as textile dyes. In a typical experiment, an aqueous dye solution (1.0 mM) and $NaBH_4$ (10.0 mM) were added to the Ag_2O NPs/Alg-Hy composite (1.0 mL) in a vial. The mixture was gently shaken and then allowed to stand under ambient conditions. Aliquots were collected at certain time intervals for analytical measurements. The absorbance spectra were recorded using a UV-visible spectrophotometer. As a control, the absorbance of the dye solution without the catalyst was measured under identical conditions. After the completion of each catalytic cycle, the reduced dye solution was decanted, and a fresh mixture of dye and $NaBH_4$ (*vide infra*) was added to the same vial to initiate the next cycle.

Kinetics of dye degradation. $NaBH_4$ (10.0 mM) was mixed with an aqueous solution of CR, MO or mixture of dyes (CR and MO) to study the degradation process (*vide infra*). The reduction followed pseudo first order kinetics and the following equation was used to analyse the reaction kinetics:

$$\ln\left(\frac{A_t}{A_0}\right) = -kt$$

where, k = pseudo 1st order rate constant, t = reaction time, A_t = absorbance of the dye at time t, and A_0 = absorbance of the dye at the time $t = 0$.

Quantitative analysis of dye degradation. The degradation efficiency of CR and MO dyes was calculated using the following formula:

$$\%\ \text{Degradation} = \frac{A_0 - A_t}{A_0} \times 100$$

where, A_0 = the initial absorbance dye solution before treatment, and A_t = the absorbance of the treated solution obtained at specified time/after degradation.

Results and discussion

Catalytic control over Alg-Hy preparation

The strategy for synthesizing Ag-based NPs within an alginate-based hydrogel matrix is guided by the following considerations: (i) the hydrogel should form under ambient conditions and would provide suitable space for nucleation and growth of the Ag-based NPs, thereby enabling control over their size and morphology, (ii) the embedded Ag-based NPs should remain stable within the hydrogel matrix, minimizing agglomeration, (iii) the combination of Ag-based NPs and the hydrogel network is expected to exhibit synergistic and unique properties that are not attainable from the individual components alone, and (iv) the synthesis process should be straightforward and yield a biocompatible material, making it suitable for applications in biomedicine and environmental remediation.

Following these design principles, we first synthesized the alginate-based hydrogel (Alg-Hy, Fig. 2a) *in situ* by mixing aqueous solutions of two components. Modified sodium alginate (Alg-A), containing aldehyde functionalities on its backbone (Scheme S1), was used in combination with guanidine hydrazine (GH, Fig. 2a and Scheme S2) as a crosslinker. Both Alg-A and GH were water-soluble and formed colourless solutions. Upon mixing at room temperature, a hydrogel (Scheme S3) was formed *via* a reaction between the aldehyde groups of Alg-A and the hydrazine groups of GH, resulting in the formation of hydrazone bond. Notably, the formation of these hydrazone bonds can be modulated through acid catalysis.[31,32]

Formation of hydrogel material was significantly influenced by the pH of the reaction medium. At pH 5 (0.1 M phosphate buffer), hydrogel formation was rapid, with gelation occurring within approximately 140 minutes. In contrast, at pH 7 (0.1 M phosphate buffer), gelation required approximately 12 hours. Furthermore, the minimum gelation concentration (MGC) of GH required to form a stable hydrogel with 1.0 wt% Alg-A was 28 mM at pH 5, compared to 40 mM at pH 7 (Table S1). These results are consistent with the acid-catalysed mechanism of hydrazone bond formation between the aldehyde groups of Alg-A and the hydrazine functionalities of GH.[33,34] The presence of H^+ ions at pH 5 facilitated faster crosslinking, resulting in accelerated hydrogel formation. Conversely, in the near-neutral environment at pH 7, the absence of acid catalysis led to slower reaction kinetics and delayed gelation. To investigate the surface morphology of the hydrogel materials, field emission scanning electron microscopy (FESEM) was performed. The hydrogel prepared at pH 5 exhibited a disk-like structure with a rough, heterogeneous surface (Fig. 2b), whereas the hydrogel formed at pH 7 displayed a more homogeneous surface characterized by an interconnected fibrous network (Fig. 2c). Rheological analysis was conducted to evaluate the viscoelastic properties of the hydrogels. The hydrogel synthesized at pH 7 (1.0 wt% Alg-A, 50 mM GH) exhibited a higher storage modulus (~500 Pa), indicating a mechanically stronger material. In contrast, the hydrogel prepared at pH 5 showed a significantly

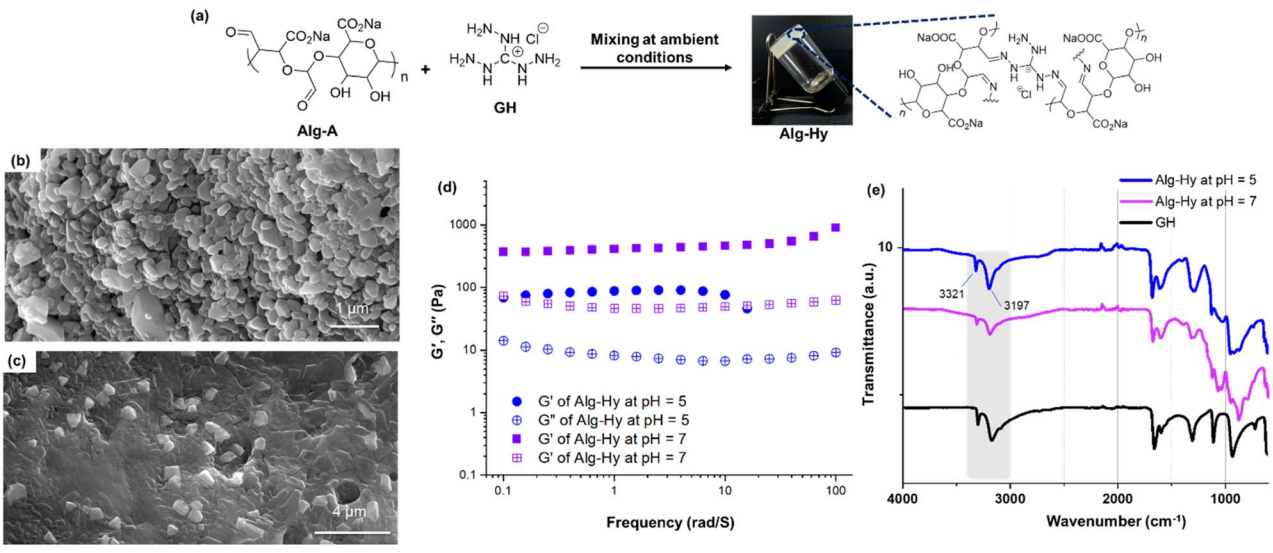

Fig. 2 *In situ* preparation of the Alg-Hy material. (a) Schematic representation of hydrazone-based Alg-Hy formation *via* mixing aqueous solutions of Alg-A and GH. (b and c) FESEM images of Alg-Hy prepared at (b) pH 5 (scale bar: 1 μm), and (c) pH 7 (scale bar: 4 μm), showing differences in surface morphology. (d) Rheological analysis of Alg-Hy hydrogels prepared at pH 5 (circles) and pH 7 (rectangles), indicating variation in mechanical strength. (e) FTIR spectra of Alg-Hy prepared at pH 5 (purple), pH 7 (pink), in comparison with GH (black).

lower storage modulus (~100 Pa) (Fig. 2d). This difference is likely due to the faster reaction kinetics at acidic pH, which may lead to partial and inhomogeneous crosslinking. In contrast, the slower gelation process at neutral pH allows for more uniform and extended network formation, resulting in enhanced mechanical properties. Fourier-transform infrared (FTIR) spectroscopy provided further insights into the network structure. Characteristic N–H stretching bands associated with unreacted hydrazine groups were observed around 3321 cm^{-1} and 3197 cm^{-1} (Fig. 2e). These peaks were more pronounced in the hydrogel formed at pH 5, suggesting incomplete consumption of the hydrazine groups under acidic conditions. In contrast, fewer unreacted hydrazine functionalities were observed in the hydrogel formed at pH 7, indicating a more complete crosslinking process. Collectively, these results demonstrate that the properties of the hydrazone-based hydrogel (Alg-Hy) can be effectively tuned by adjusting the pH of the reaction medium. The degree of crosslinking, network morphology, and mechanical strength are all governed by the rate of hydrazone bond formation, which is pH-dependent.

In situ preparation of Ag_2O NPs/Alg-Hy composite material

We envisioned that the unreacted hydrazine functionalities of GH could serve as active sites for further functionalization, such as the *in situ* formation of metal-based NPs within the hydrogel network. To explore this, silver nitrate ($AgNO_3$) was incorporated as an additional precursor during the mixing of Alg-A and GH, whereby GH served both as a reducing agent for the *in situ* formation of silver-based nanoparticles and as a crosslinker for the alginate chains. Initially, the addition of $AgNO_3$ to the phosphate buffer solution led to the formation of a brown precipitate. To this end, deionized water was used instead of buffer to prepare the aqueous solutions of the building blocks. Upon mixing Alg-A, GH, and $AgNO_3$ under ambient conditions (Fig. 3a, and Scheme S4), an opaque hydrogel formed, which gradually turned pale yellow over time (Fig. 3b and Video SV1). This colour change suggested the formation of Ag_2O nanoparticles (NPs) within the hydrogel matrix. The individual aqueous solutions of Alg-A and GH were neutral (pH = 7), whereas $AgNO_3$ solution was acidic (pH = 5). The mixture of all three components yielded an acidic pH (~5), thus providing acidic conditions that catalysed the formation of hydrazone bonds. The observed transformation, from opaque to pale yellow material over time, indicated that hydrazone crosslinking occurred faster than the formation of Ag_2O NPs.

FTIR spectroscopy confirmed hydrazone bond formation in the Ag_2O NPs/Alg-Hy material (Fig. 3c). The characteristic aldehyde peak of Alg-A at 1612 cm^{-1} disappeared, while a new band corresponding to C–N stretching appeared at 1684 cm^{-1}, indicating successful hydrazone linkage formation. Ultraviolet-visible (UV-Vis) spectroscopy further supported Ag_2O NP formation, as the composite hydrogel showed a distinct

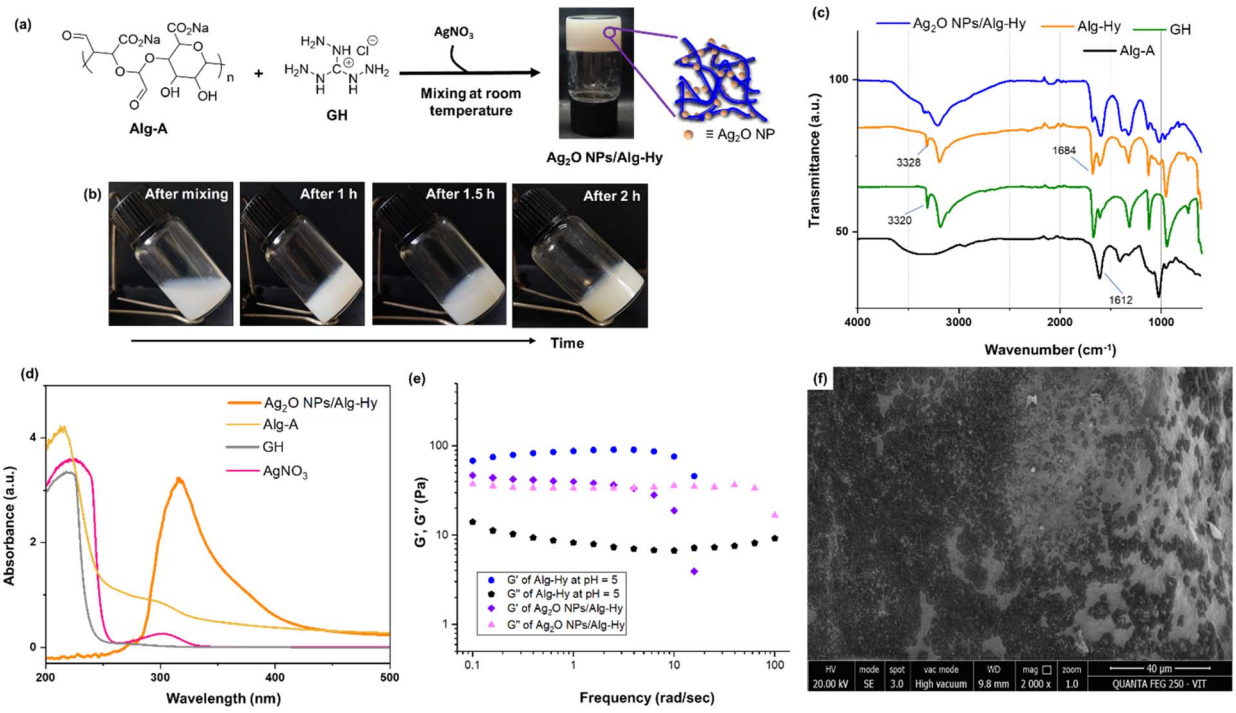

Fig. 3 Preparation and characterization of Ag_2O NPs/Alg-Hy composite material. (a) Schematic representation of the *in situ* synthesis of Ag_2O NPs/Alg-Hy by mixing aqueous solutions of Alg-A, GH, and $AgNO_3$ at room temperature. (b) Photographs showing the appearance of the material at different time intervals. (c) FTIR spectra of Ag_2O NPs/Alg-Hy (violet), compared with its individual components: Alg-Hy (orange), GH (green), and Alg-A (black). (d) UV-Vis absorption spectra of Ag_2O NPs/Alg-Hy (orange), Alg-A (yellow), GH (grey), and $AgNO_3$ (pink), indicating successful incorporation of silver species. (e) Rheological analysis (frequency sweep at 1% strain) comparing Ag_2O NPs/Alg-Hy and Alg-Hy prepared at pH 5. (f) FESEM image of Ag_2O NPs/Alg-Hy, showing the surface morphology (scale bar: 40 µm).

absorption maximum at 325 nm, absent in the spectra of the individual components (Fig. 3d). A concentration of 30 mM $AgNO_3$ was found to be optimal, as further increases did not enhance absorbance at 325 nm (Fig. S2), suggesting saturation in Ag_2O NP formation. Importantly, control experiments involving only $AgNO_3$ with either Alg-A or GH resulted in either no observable change (transparent solution for 3 hours) or rapid precipitation (white AgCl within 2 minutes), indicating that the hydrogel matrix plays a critical role in controlling nanoparticle formation and stabilization. Hence, 30 mM $AgNO_3$ was used in subsequent studies unless otherwise stated. The presence of Ag_2O NPs within the Alg-Hy network did not disrupt hydrogel formation. FTIR analysis showed that the hydrazone bond structure remained unchanged upon incorporation of nanoparticles. However, rheological measurements revealed that the Ag_2O NPs/Alg-Hy composite exhibited lower mechanical strength compared to the Alg-Hy prepared at pH 5 (Fig. 3e). FESEM revealed a layered structure for the Ag_2O NPs/Alg-Hy material, similar to that observed for Alg-Hy at pH 5 (Fig. 3f, and Fig. S3). Numerous bright spots were observed, indicative of embedded nanoparticles. Energy-dispersive X-ray (EDX) spectroscopy confirmed the presence of silver along with carbon, nitrogen, oxygen, and chlorine in the composite (Fig. S4), and elemental mapping verified uniform silver distribution within the hydrogel matrix (Fig. S5).

Transmission electron microscopy (TEM) was used to determine the nanoparticle size distribution (Fig. 4a), revealing average particle diameters of approximately 10 nm. High-resolution TEM (HRTEM) images showed interplanar spacings of 3.04 Å (Fig. 4b). X-ray diffraction (XRD) patterns further confirmed the formation of crystalline Ag_2O within the Alg-Hy hydrogel. While Alg-Hy alone exhibited an amorphous pattern (Fig. 4c, black line), the Ag_2O NPs/Alg-Hy composite showed sharp diffraction peaks at 28.1°, 32.5°, 46.5°, 55.2°, and 57.8°, corresponding to the (110), (111), (211), (220), and (310) planes of cubic Ag_2O, as per JCPDS file no. 01-076-1393 (ref. 35 and 36) (Fig. 4c, purple line). The intense peak at 32.5° suggested preferential orientation. The average crystallite size, calculated using the Debye–Scherrer equation, was ~16 nm, consistent with TEM data. X-ray photoelectron spectroscopy (XPS) was performed to analyse surface composition (Fig. 4d). The XPS spectrum revealed prominent peaks corresponding to O 1s (531 eV), N 1s (398.8 eV), C 1s (284.2 eV), and Cl 2p (197.4 eV). In addition, characteristic signals for Ag in 3d region were observed at ~365 eV and ~372 eV, which corresponds to Ag_2O.[37,38] High-resolution XPS spectra showed two peaks at 365.8 eV and 371.5 eV, assigned to Ag $3d_{5/2}$ and Ag $3d_{3/2}$, respectively, with a spin–orbit splitting of 5.7 eV (Fig. 4e), confirming the presence of Ag(I) in the Ag_2O NPs.[39,40] Thermogravimetric analysis (TGA) was conducted to evaluate thermal stability (Fig. 4f). The Ag_2O NPs/Alg-Hy composite demonstrated enhanced thermal stability compared to Alg-Hy alone, with a 73.5% mass loss at 600 °C *versus* 81.3% for Alg-Hy. Based on the difference in organic mass loss, the Ag_2O content was estimated to be ~7.8 wt%. Brunauer–Emmett–Teller (BET) surface area analysis indicated that the Ag_2O NPs/Alg-Hy composite had a high surface area of 589.92 $m^2\ g^{-1}$, with an average pore diameter of 2.18 nm. The typical N_2 adsorption

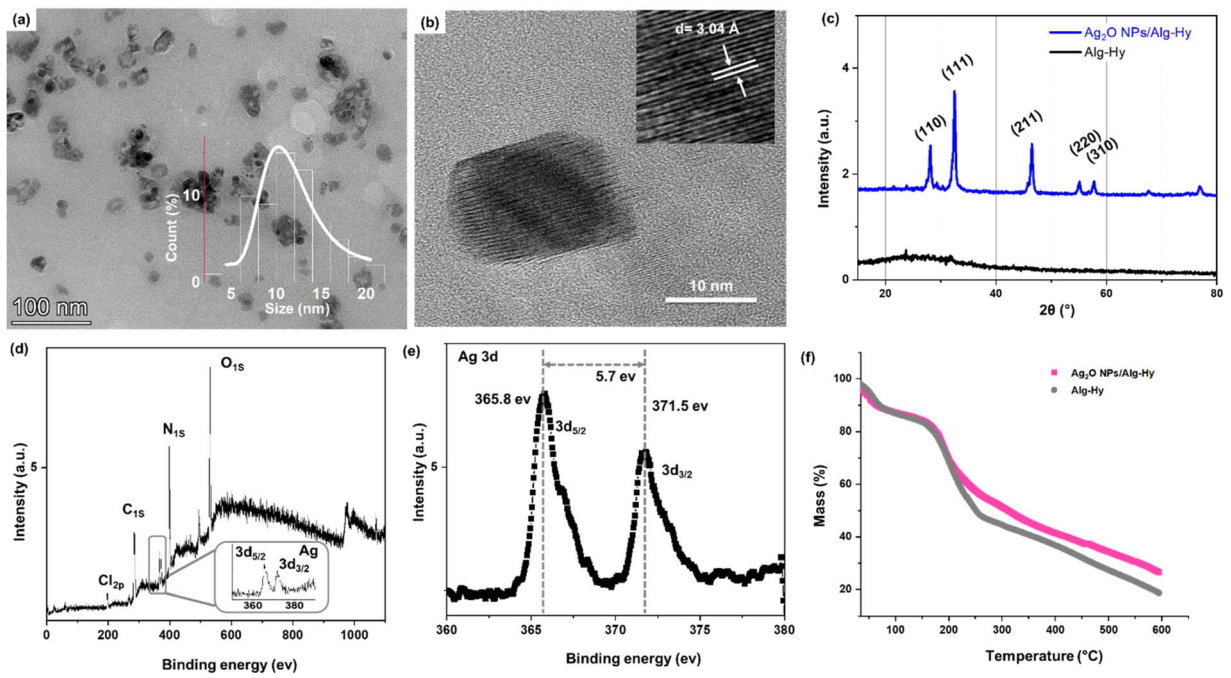

Fig. 4 Characterization of Ag_2O NPs/Alg-Hy material. (a) TEM image of Ag_2O NPs/Alg-Hy, with inset showing particle size distribution and Gaussian fitting, (b) HRTEM micrograph showing Ag_2O NPs, (c) XRD patterns of Ag_2O NPs/Alg-Hy and pristine Alg-Hy, indicating the crystalline structure of Ag_2O, (d) XPS of Ag_2O NPs/Alg-Hy, (e) HR-XPS showing spin-orbital components ($3d_{3/2}$ and $3d_{5/2}$) of Ag, and (f) TGA analysis of Ag_2O NPs/Alg-Hy (pink line) and Alg-Hy (grey line) demonstrating thermal stability of the composite.

isotherms of Ag_2O NPs/Alg-Hy showed a superimpose adsorption and desorption isotherms (Fig. S6), indicating the adsorption of the samples mostly occurred in the micropores.

These results collectively demonstrate that Ag_2O NPs can be controllably synthesized and embedded within the Alg-Hy matrix under mild, and ambient conditions. Furthermore, the system allows for tuneable nanoparticle loading simply by adjusting the concentration of $AgNO_3$. Hydrogel network of Alg-Hy serves as both a structural support and stabilizing matrix for *in situ* Ag_2O nanoparticle formation, supported by the reducing capability of hydrazine-functionalized crosslinker GH. Its three-dimensional porous structure confines nanoparticle growth, preventing aggregation, as confirmed by TEM analysis. This results in a stable, well-dispersed nanocomposite with strong potential for catalytic applications in environmental remediation.

Preparation of Ag NPs/Alg-Hy from Ag_2O NPs/Alg-Hy

Anthropogenic activities, particularly the direct discharge of industrial contaminants into aquatic ecosystems, have led to a rapid decline in global freshwater resources. These pollutants pose a significant environmental and public health concern, as they can bioaccumulate in the food chain, ultimately affecting human health.[41,42] Therefore, water reclamation and reuse strategies have become essential to meet the rising global demand for clean water.[43] In this context, the rapid and efficient removal of pollutants from wastewater is of paramount importance. Among various remediation strategies, nanoparticle (NP)-based heterogeneous catalysis has emerged as an environmentally benign and economically viable approach.[44–47] In particular, silver nanoparticles (Ag NPs) have gained widespread attention for the catalytic degradation of organic dyes due to their high catalytic efficiency.[48,49] However, their practical application is hindered by issues such as aggregation, poor stability, limited recyclability, high cost, and susceptibility to self-corrosion in aqueous media. To address these limitations, we proposed the use of Ag NPs embedded within the Alg-Hy hydrogel network (Ag NPs/Alg-Hy) as a stable, recyclable, and effective catalytic system for dye degradation. The hydrogel matrix not only offers a stabilizing environment that prevents NP aggregation but also allows for multiple catalytic cycles. To generate Ag NPs within the hydrogel matrix, the previously synthesized Ag_2O NPs/Alg-Hy composite was treated with aqueous sodium borohydride ($NaBH_4$). This treatment

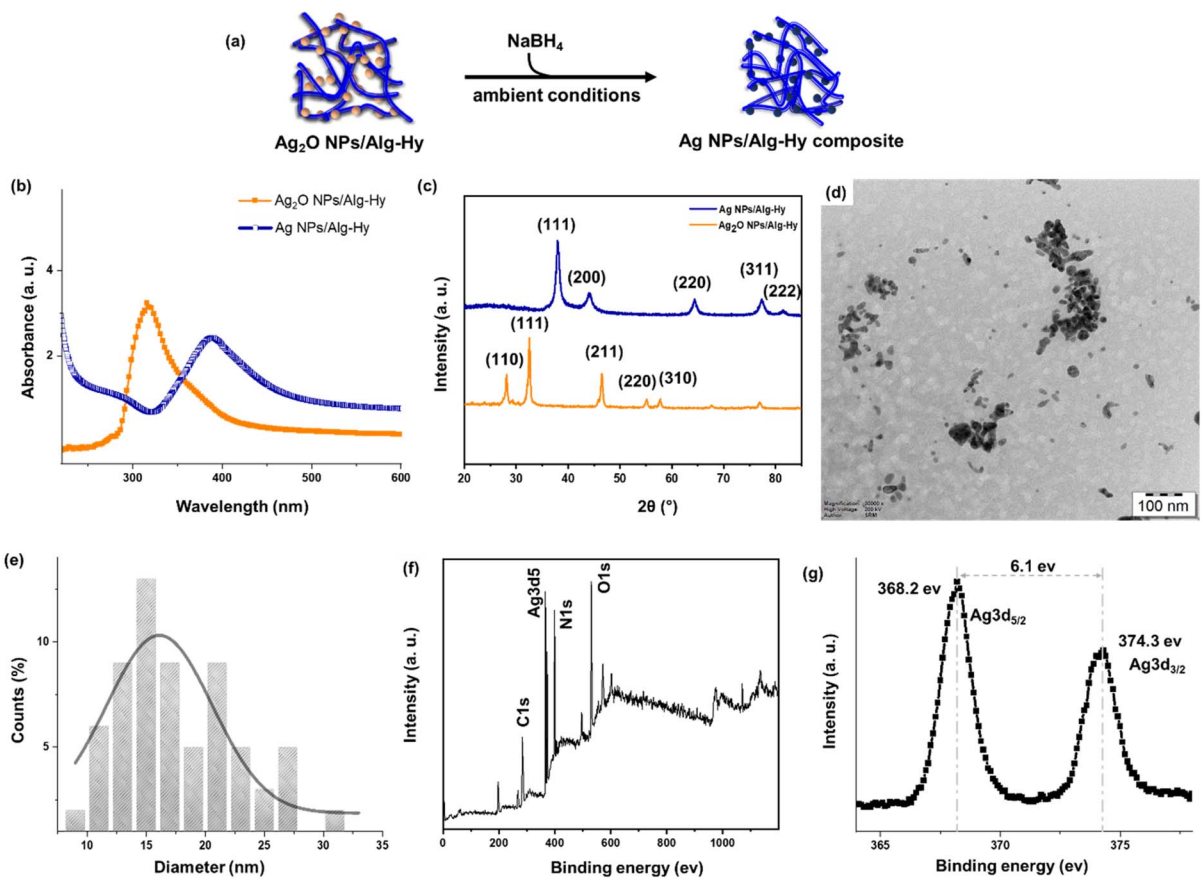

Fig. 5 Preparation of Ag NPs/Alg-Hy material. (a) A schematic for the preparation of Ag NPs/Alg-Hy composite material *via* addition of aqueous solution of $NaBH_4$ to Ag_2O NPs/Alg-Hy at room temperature, (b) comparative UV-Vis spectroscopic analysis of Ag NPs/Alg-Hy (blue line) and Ag_2O NPs/Alg-Hy (orange line), and (c) comparative XRD analysis of Ag NPs/Alg-Hy (blue line) and Ag_2O NPs/Alg-Hy (orange line). (d) TEM image of the Ag NPs/Alg-Hy material, (e) size distribution histogram with Gaussian fitting, (f) XPS of the Ag NPs/Alg-Hy, and (g) HR-XPS showing spin-orbital components ($3d_{3/2}$ and $3d_{5/2}$) of Ag.

facilitated the *in situ* reduction of Ag_2O NPs to metallic Ag NPs, as confirmed by UV-Vis spectroscopy and pXRD analyses. UV-Vis spectroscopy of the composite material after $NaBH_4$ treatment showed a distinct absorption maximum at 390 nm (Fig. 5a), corresponding to the surface plasmon resonance (SPR) of Ag NPs. In contrast, the Ag_2O NPs/Alg-Hy composite exhibited an absorption maximum at 325 nm (Fig. 5b), confirming the successful conversion of Ag_2O to Ag^0. The pXRD pattern of the resulting material revealed sharp diffraction peaks at 38.1°, 44.1°, 64.3°, 77.3°, and 81.5°(Fig. 5c), which correspond to the (111), (200), (220), (311), and (222) planes of face-centered cubic (fcc) metallic silver, in agreement with JCPDS file no. 00-004-0783.[50–52] These results confirmed the crystalline nature of the *in situ*-formed Ag NPs. TEM was used to examine the size and morphology of the Ag NPs (Fig. 5d). The average particle size was determined to be ~15 nm, which is slightly larger than that of the precursor Ag_2O NPs (Fig. 5e). XPS was also performed to analyse the surface composition of the Ag NPs/Alg-Hy composite (Fig. 5f). While the survey spectrum appeared similar to that of the Ag_2O NPs/Alg-Hy, the high-resolution XPS spectra in the Ag 3d region displayed two distinct peaks at 368.2 eV and 374.3 eV, corresponding to the Ag $3d_{5/2}$ and Ag $3d_{3/2}$ orbitals, respectively, with a spin–orbit splitting of 6.1 eV (Fig. 5g). This energy separation is characteristic of metallic Ag(0), confirming the successful formation of zero-valent silver nanoparticles.[53,54]

Catalytic dye degradation

Degradation of Congo red. To evaluate the catalytic potential of the Ag NPs/Alg-Hy composite in aqueous media, we investigated its performance in the degradation of organic dyes. We hypothesized that the addition of aqueous $NaBH_4$ would facilitate the *in situ* generation of catalytically active Ag NPs, which would act both as electron mediators and as a source of hydride ions (H^-) for the reduction of organic pollutants such as azo dyes. Congo red (CR), a widely used azo dye known for its high toxicity to animals and carcinogenic potential in humans, was chosen as a model pollutant. Its efficient removal from industrial effluents is of significant environmental importance.[55,56] To monitor the degradation process, we recorded UV-Vis absorption spectra of an aqueous CR solution (1.0 mM) mixed with Ag_2O NPs/Alg-Hy and $NaBH_4$ (10 mM). A distinct visual color change from red to colorless was observed within 5 minutes, indicating rapid decolorization (Fig. 6a). The degradation process was further confirmed by time-dependent UV-Vis spectral analysis (Fig. S7). The complete decolorization of CR occurred within 5 minutes in the presence of both Ag_2O NPs/Alg-Hy and $NaBH_4$. In contrast, control experiments showed significantly slower degradation: over 6 hours in the presence of $NaBH_4$ alone and similarly prolonged in the presence of Ag_2O NPs/Alg-Hy alone (Fig. 6b). These results suggest a synergistic effect between the hydrogel-embedded Ag NPs and the reducing agent. Kinetic analysis revealed that the CR degradation followed pseudo-first-order kinetics, with a rate constant of 0.79 min^{-1} when both Ag_2O NPs/Alg-Hy and $NaBH_4$ were present. In comparison, the rate constants for control reactions using only Ag_2O NPs/Alg-Hy or $NaBH_4$ were significantly lower (0.001 min^{-1} and 0.0008 min^{-1}, respectively; Table S2). Over 95% of the dye was degraded within 5 minutes under catalytic conditions, whereas only ~30% degradation occurred over 360 minutes in the control setups.

The enhanced degradation efficiency is attributed to the *in situ* formation of Ag NPs, which promote effective electron transfer from BH_4^- ions (electron donors) to the dye molecules (electron acceptors).[57] The proposed mechanism involves adsorption of BH_4^- onto the Ag NP surface, followed by electron transfer to the dye, facilitating its reduction. The high surface area of Ag NPs likely contributes to the increased rate of decolorization. To confirm dye degradation and identify the resulting products, mass spectrometric (MS) analysis was performed. The MS spectrum of the degraded solution exhibited peaks at *m*/*z* values of 316, 184, 158, and 130 (Fig. S8). The absence of high-molecular-weight fragments and the appearance of multiple low-mass peaks suggest cleavage of the azo and sulfonate groups of CR. A proposed fragmentation pathway is presented in Fig. S9.

The recyclability of the composite material was also evaluated, as this is a critical parameter for practical applications.[58] A fresh CR solution (1.0 mM) was treated with Ag_2O NPs/Alg-Hy (1.0 mL) and $NaBH_4$ (10.0 mM), and complete decolorization was again observed within 5 minutes. After each cycle, the solution was filtered, and the recovered composite was reused with a fresh dye and $NaBH_4$ solution. The reusability was monitored by UV-Vis spectroscopy, tracking the absorbance at 500 nm (Fig. 6c). The composite retained its catalytic efficiency for at least nine consecutive cycles, achieving ~96% degradation. However, a noticeable increase in the reaction time (>5 minutes) was observed after the ninth cycle, likely due to partial nanoparticle agglomeration or leaching of Ag NPs from the hydrogel matrix (*vide infra*).

Degradation of methyl orange. The dye degradation performance of the Ag NPs/Alg-Hy composite was further evaluated using methyl orange (MO), another representative azo dye. UV-Vis spectroscopy was employed to monitor the decolorization process (Fig. 6d). Upon treatment with Ag_2O NPs/Alg-Hy in the presence of aqueous $NaBH_4$ (10.0 mM), a 1.0 mM aqueous solution of MO exhibited a rapid colour change from orange to colourless within 5 minutes (Fig. S10). The degradation kinetics followed a pseudo-first-order reaction with a rate constant of 0.78 min^{-1} (Table S3). Approximately 99% of the MO was degraded within 5 minutes under catalytic conditions, whereas control experiments showed only ~13% degradation in the presence of $NaBH_4$ alone and ~3% in the presence of Ag_2O NPs/Alg-Hy alone after 360 minutes (Fig. 6e, and Table S3). The corresponding rate constants for these control conditions were significantly lower (0.0002 min^{-1}, and 0.0001 min^{-1} respectively), highlighting the synergistic role of both the composite material and the reducing agent in achieving efficient dye degradation. MS analysis of the degraded solution further confirmed the breakdown of the MO dye. The MS spectrum exhibited prominent peaks at *m*/*z* 133, 96.4, and 80 (Fig. S11), with the absence of high-molecular-weight fragments. This indicates the cleavage of the azo bond and formation of lower-

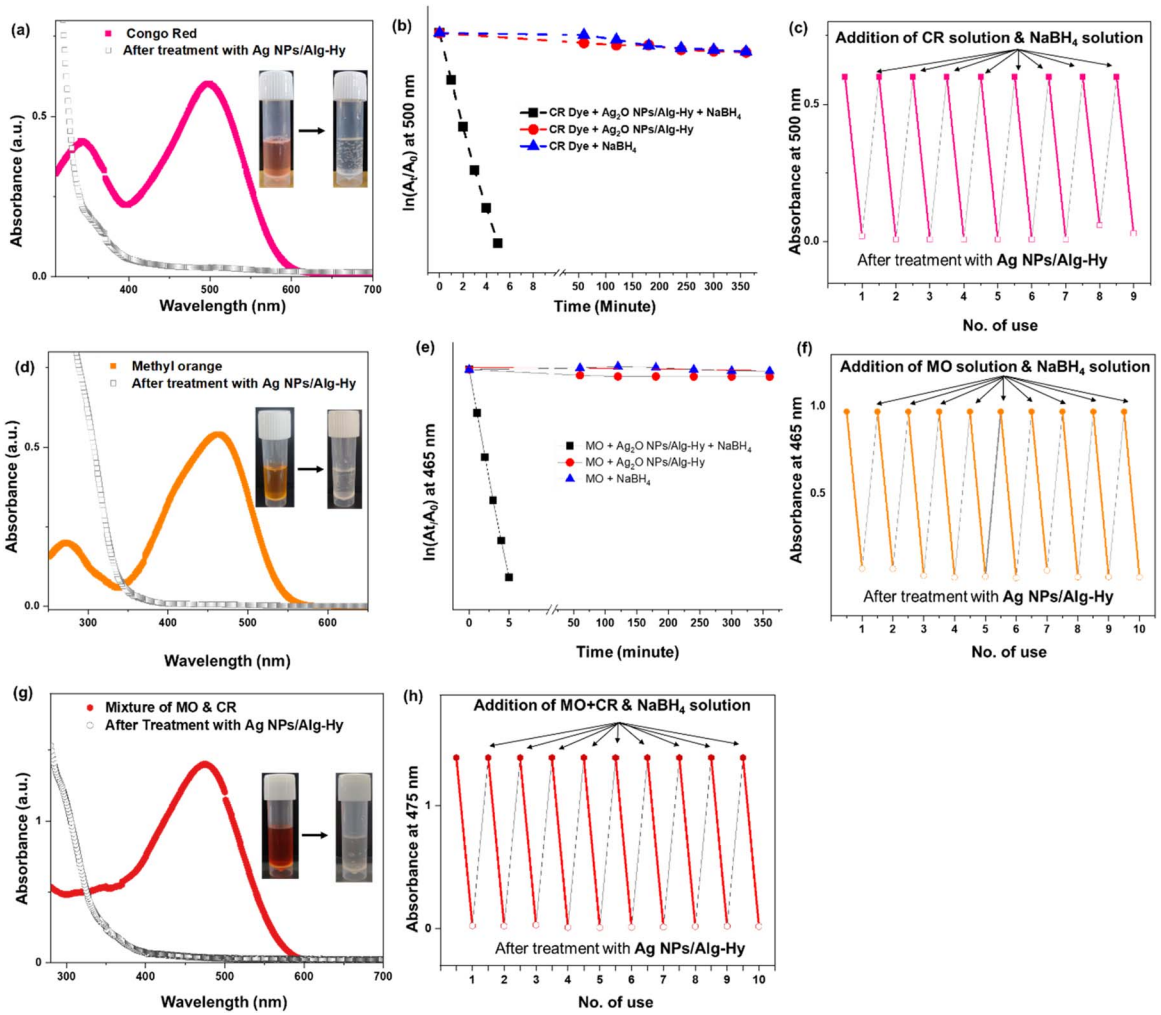

Fig. 6 Dye degradation with the Ag NPs/Alg-Hy composite material. (a) Optical absorbance spectra of CR solution, (b) relative rate of CR dye degradation in presence of Ag_2O NPs/Alg-Hy material and $NaBH_4$ (black square), only in presence of Ag_2O NPs/Alg-Hy material (red circle), and only in presence of $NaBH_4$ (blue triangle), (c) recyclability test of the composite material for CR degradation following the absorbance at 500 nm, (d) optical absorbance spectra of MO solution, (e) relative rate of MO dye degradation in presence of Ag_2O NPs/Alg-Hy material, and $NaBH_4$ (black square), only in presence of Ag_2O NPs/Alg-Hy material (red circle), and only in presence of $NaBH_4$ (blue triangle), (f) recyclability test of the composite material for MO dyes following the absorbance at 463 nm, (g) optical absorbance spectra of mixture of CR and MO dyes before and after the treatment with the composite material, (h) recyclability test of the composite for mixture of CR and MO dyes following the absorbance at 475 nm. Lines in b, c, e, f and h are drawn to guide the eyes.

mass degradation products.[59] To assess the recyclability of the composite material, repeated dye degradation cycles were conducted. In each cycle, the MO solution (1.0 mM) was treated with Ag_2O NPs/Alg-Hy (1.0 mL) and $NaBH_4$ (10.0 mM), followed by filtration of the decolorized solution and reuse of the composite material with fresh reagents. UV-Vis spectroscopy was used to monitor the absorbance at 465 nm (Fig. 6f). The composite retained its catalytic activity over more than 10 successive cycles, maintaining a degradation efficiency of ~96%.

To investigate the observed decline in degradation efficiency after the 10th cycle, FESEM analysis of the used composite was performed. The images revealed that while the hydrogel maintained a layered morphology (Fig. S12), significant nanoparticle agglomeration into larger clusters was observed. This aggregation likely reduced the effective surface area available for catalysis. Additionally, partial loss of nanoparticles during filtration steps may have contributed to the reduced activity. While the possibility of Ag NP leaching into the aqueous medium cannot be excluded, a quantitative evaluation of silver release is required to assess long-term environmental safety, an aspect identified for future study.

Finally, the dye degradation performance of the Ag NPs/Alg-Hy system was compared with other reported catalyst systems (Table S4).[60–62] The present method, which enables the preparation of the composite material under mild, ambient conditions, stands out for its operational simplicity, high catalytic efficiency in aqueous media, and excellent recyclability across multiple cycles.

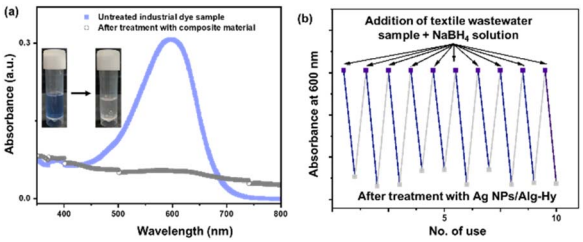

Fig. 7 Degradation of textile wastewater using the composite material. (a) UV-Vis absorbance spectra of the textile wastewater sample before (blue line) and after the treatment with composite material (grey line). Inset: photographs of the wastewater sample before and after treatment. (b) Recyclability of the composite material evaluated over multiple cycles by monitoring absorbance at 600 nm.

Degradation of dye mixture. To further validate the applicability of our composite material for real-world wastewater treatment, we investigated its performance in degrading a mixed dye solution, as actual industrial effluents often contain multiple dye pollutants.[53] A mixture of Congo red (CR, 1.0 mM) and methyl orange (MO, 1.0 mM) was prepared and treated with the Ag NPs/Alg-Hy composite. Upon treatment, a distinct colour change from dark red to colourless was observed, indicating successful degradation. The decolorization process was monitored *via* UV-Vis spectroscopy (Fig. 6g), which showed complete degradation of the dye mixture within 5 minutes under ambient conditions. The recyclability of the composite was also assessed for the mixed dye system. The material maintained high catalytic efficiency (~98%) over 10 consecutive degradation cycles without significant loss of activity (Fig. 6h). These findings further support the suitability of the Ag NPs/Alg-Hy composite for practical wastewater remediation, offering rapid, efficient, and reusable dye degradation under mild, environmentally friendly conditions. It is noteworthy that all catalytic experiments were performed under consistent laboratory ambient conditions, and natural light was found to have no appreciable effect on the degradation process.

Degradation of real textile wastewater. To evaluate the real-world applicability of the Ag NPs/Alg-Hy composite, wastewater samples were collected from a textile industry in Salem, Tamil Nadu, and used directly in laboratory experiments to assess the degradation efficiency of the composite material. Upon treatment with the Ag_2O NPs/Alg-Hy composite in the presence of $NaBH_4$, a rapid colour change from navy blue to colourless was observed within 5 minutes. The degradation process was monitored using UV-Vis spectroscopy (Fig. 7a). The composite material demonstrated good reusability, maintaining approximately 82% degradation efficiency over 10 cycles (Fig. 7b). These findings highlight the potential of the composite material as a highly effective, reusable, and sustainable material for textile wastewater treatment under ambient condition.

Conclusions

In summary, we have developed a facile, one-pot, ambient-condition method for the preparation of Ag_2O nanoparticle (NP)-embedded biopolymer-based hydrogel composite. The hydrogel matrix (Alg-Hy) was formed *in situ* through hydrazone bond formation between aldehyde-functionalized alginate (Alg-A) and guanidine hydrazine (GH), where GH crosslinked the alginate chains. Hydrogelation and the properties of hydrogel was tuneable *via* acid catalysis. Acidic conditions significantly accelerated hydrogel formation, while neutral pH led to slower, uncatalyzed crosslinking. Importantly, the unreacted hydrazine functionalities within the hydrogel network provided reactive sites for further functionalization. We demonstrated the *in situ* formation of Ag_2O NPs within the hydrogel matrix by simply mixing aqueous solutions of Alg-A, GH, and $AgNO_3$. This eliminates the need for external reducing or stabilizing agents, surfactants, or specialized equipment (*e.g.*, heat, light, or ultrasound). This templated-growth strategy effectively prevented nanoparticle aggregation and enabled direct preparation of the composite material at the point of application. Subsequent reduction of Ag_2O NPs to Ag NPs using aqueous $NaBH_4$ generated a catalytically active composite (Ag NPs/Alg-Hy), which was employed for the rapid degradation of organic dyes in water. Model azo dyes such as Congo red (CR), methyl orange (MO), their mixtures, and textile wastewater sample were efficiently degraded within 5 minutes. The composite also exhibited excellent reusability over multiple degradation cycles without significant loss of activity.

Overall, this work presents a simple, scalable, and environmentally benign method for fabricating nanoparticles-embedded hydrogel composite under ambient conditions. The strategy holds significant promise for environmental remediation, particularly for dye-laden industrial wastewater, and could be extended to incorporate various biopolymers and (non-)metallic nanoparticles for broader applications, including those in resource-limited settings or biomedical contexts.

Author contributions

C. M., D. J., A. M., and N. D. conceived the idea. D. J., N. D., and C. M. designed the experiments. D. J., and N. D. performed the experiments. C. M. supervised the research and wrote the manuscript. All authors analysed the data, commented on the manuscript, and have given approval to the final version of the manuscript.

Conflicts of interest

A part of this work has been filed as Indian patent application (application no.: IN202441040131) with all the authors as inventor.

Data availability

The data that support the findings of this study are openly available in figshare at **https://doi.org/10.6084/m9.figshare.29087996.v1**.

Additional schemes, tables, and graphical data supporting the findings of this study are available in the SI. See DOI: https://doi.org/10.1039/d5ra03595c.

Acknowledgements

C. M. acknowledges the funding from Vellore Institute of Technology as a seed grant (no. SG20240013), and N. D. thanks Department of Science and Technology (DST), Govt. Of India for an INSPIRE fellowship (no. DST/INSPIRE/03/2022/000179). All authors acknowledge the central instrumental facility of VIT Vellore to carry out the work. Authors thank Prof. Suryasarathi Bose, Mr Samir Mondal (IISC, Bangalore) for the help in rheology measurement, and Prof. Vijayaraghavan R. and Mr Harikaran Dhakshnamoorthi (Chemistry Dept., VIT Vellore) for the help in TGA measurement.

References

1 M. F. Matus and H. Häkkinen, *Nat. Rev. Mater.*, 2023, **8**, 372, DOI: 10.1038/s41578-023-00537-1.
2 V. S. Raghuwanshi and G. Garnier, *Adv. Funct. Mater.*, 2025, **35**, 2412869, DOI: 10.1002/adfm.202412869.
3 Z. Yu, Y. Gu, Y. Ren, Z. Li, C. Mou, Z. Wu, D. Wu and J. Mou, *J. Mater. Chem. C*, 2024, **12**, 16646, DOI: 10.1039/D4TC03610G.
4 H. Dawit, Y. Zhao, J. Wang and R. Pei, *Biomater. Sci.*, 2024, **12**, 2786, DOI: 10.1039/D4BM00048J.
5 Y. Shi, X. Han, S. Zou and G. Liu, *ACS Nano*, 2024, **18**, 33276–33292, DOI: 10.1021/acsnano.4c13330.
6 T. K. Das, M. Jesionek, Y. Çelik and A. Poater, *Sci. Total Environ.*, 2023, **901**, 165772, DOI: 10.1016/j.scitotenv.2023.165772.
7 J. Dadashi, M. A. Ghasemzadeh and M. Salavati-Niasari, *RSC Adv.*, 2022, **12**, 23481–23502, DOI: 10.1039/D2RA03418B.
8 A. T. Silva, R. Figueiredo, M. Azenha, P. A. Jorge, C. M. Pereira and J. A. Ribeiro, *ACS Sensors*, 2023, **8**, 2898–2920, DOI: 10.1021/acssensors.3c01010.
9 K. Y. Wong, Z. Nie, M. S. Wong, Y. Wang and J. Liu, *Adv. Mater.*, 2024, **36**, 2404053, DOI: 10.1002/adma.202404053.
10 N. Kumar, R. Gusain, S. Pandey and S. S. Ray, *Adv. Mater. Interfaces*, 2023, **10**, 2201375, DOI: 10.1002/admi.202201375.
11 P. Thoniyot, M. J. Tan, A. A. Karim, D. J. Young and X. J. Loh, *Adv. Sci.*, 2015, **2**, 1400010, DOI: 10.1002/advs.201400010.
12 C. Marambio-Jones and E. M. Hoek, *J. Nanoparticle Res.*, 2010, **12**, 1531–1551, DOI: 10.1007/s11051-010-9900-y.
13 A. J. Clasky, J. D. Watchorn, P. Z. Chen and F. X. Gu, *Acta Biomater.*, 2021, **122**, 1, DOI: 10.1016/j.actbio.2020.12.030.
14 S. S. Sana, R. Haldhar, J. Parameswaranpillai, M. Chavali and S. C. Kim, *Clean. Mater.*, 2022, **6**, 100161, DOI: 10.1016/j.clema.2022.100161.
15 Y. Guo, V. Walter, S. Vanuytsel, C. Parperis, J. T. Sengel, E. E. Weatherill and M. I. Wallace, *J. Am. Chem. Soc.*, 2023, **145**, 15809, DOI: 10.1021/jacs.3c02484.
16 M. A. Huq, M. Ashrafudoulla, M. M. Rahman, S. R. Balusamy and S. Akter, *Polymers*, 2022, **14**, 742, DOI: 10.3390/polym14040742.
17 S. S. Yilmaz and A. Aytac, *J. Polym. Res.*, 2022, **29**, 473, DOI: 10.1007/s10965-022-03309-7.
18 A. Sharma, C. Verma, S. Mukhopadhyay, A. Gupta and B. Gupta, *ACS Appl. Nano Mater.*, 2022, **5**, 8546–8556, DOI: 10.1021/acsanm.2c01959.
19 Y. Ziai, C. Rinoldi, P. Nakielski, L. De Sio and F. Pierini, *Curr. Opin. Biomed. Eng.*, 2022, **24**, 100413, DOI: 10.1016/j.cobme.2022.100413.
20 P. Nezhad-Mokhtari, M. Ghorbani, L. Roshangar and J. S. Rad, *Eur. Polym. J.*, 2019, **117**, 64, DOI: 10.1016/j.eurpolymj.2019.05.004.
21 N. Das and C. Maity, *ACS Catal.*, 2023, **13**, 5544, DOI: 10.1021/acscatal.3c00411.
22 A. Moreno and M. H. Sipponen, *Mater. Horiz.*, 2020, **7**, 2237, DOI: 10.1039/D0MH00798F.
23 I. J. Budiarso, N. D. W. Rini, A. Tsalsabila, M. D. Birowosuto and A. Wibowo, *ACS Biomater. Sci. Eng.*, 2023, **9**, 3084, DOI: 10.1021/acsbiomaterials.3c00216.
24 H. Nawaz, X. Zhang, S. Chen, T. You and F. Xu, *Carbohydr. Polym.*, 2021, **267**, 118135, DOI: 10.1016/j.carbpol.2021.118135.
25 C. Maity and N. Das, *Top. Curr. Chem.*, 2022, **380**, 3, DOI: 10.1007/s41061-021-00360-8.
26 M. Kaushik and A. Moores, *Green Chem.*, 2016, **18**, 622–637, DOI: 10.1039/C5GC02500A.
27 M. Chen, Y. G. Feng, X. Wang, T. C. Li, J. Y. Zhang and D. J. Qian, *Langmuir*, 2007, **23**, 5296, DOI: 10.1021/la700553d.
28 N. Vigneshwaran, R. P. Nachane, R. H. Balasubramanya and P. V. Varadarajan, *Carbohydr. Res.*, 2006, **341**, 2012, DOI: 10.1016/j.carres.2006.04.042.
29 R. Raho, F. Paladini, F. A. Lombardi, S. Boccarella, B. Zunino and M. Pollini, *Mater. Sci. Eng. C*, 2015, **55**, 42, DOI: 10.1016/j.msec.2015.05.050.
30 S. Horikoshi, T. Sumi and N. Serpone, *Chem. Eng. Process.*, 2013, **73**, 59, DOI: 10.1016/j.cep.2013.07.009.
31 E. T. Kool, D. H. Park and P. Crisalli, *J. Am. Chem. Soc.*, 2013, **135**, 17663, DOI: 10.1021/ja407407h.
32 D. K. Kölmel and E. T. Kool, *Chem. Rev.*, 2017, **117**, 10358, DOI: 10.1021/acs.chemrev.7b00090.
33 J. Boekhoven, J. M. Poolman, C. Maity, F. Li, L. van der Mee, C. B. Minkenberg, E. Mendes, J. H. van Esch and R. Eelkema, *Nat. Chem.*, 2013, **5**, 433, DOI: 10.1038/nchem.1617.
34 D. Ramimoghadam, D. J. Eyckens, R. A. Evans, G. Moad, S. Holmes and R. Simons, *Chem.–Eur. J.*, 2024, **30**, e202401728, DOI: 10.1002/chem.202401728.
35 I. Kumar, B. Yaseen, C. Gangwar, R. Yadav, S. K. Mishra and R. M. Naik, *Mater. Today: Proc.*, 2021, **46**, 2330, DOI: 10.1016/j.matpr.2021.04.403.
36 D. G. Jeung, M. Lee, S. M. Paek and J. M. Oh, *Nanomater*, 2021, **11**, 455, DOI: 10.3390/nano11020455.
37 R. Sharma, A. Dhillon and D. Kumar, *Sci. Rep.*, 2018, **8**, 5189, DOI: 10.1038/s41598-018-23469-1.
38 S. E. Laouini, A. Bouafia, A. V. Soldatov, H. Algarni, M. L. Tedjani, G. A. M. Ali and A. Barhoum, *Membranes*, 2021, **11**, 468, DOI: 10.3390/membranes11070468.

39 H. Wang, J. Li, M. Zhou, Q. Guan, Z. Lu, P. Huo and Y. Yan, *J. Ind. Eng. Chem.*, 2015, **30**, 64, DOI: 10.1016/j.jiec.2015.05.002.
40 Z. Yang, C. Ho and S. Lee, *Appl. Surf. Sci.*, 2015, **349**, 609, DOI: 10.1016/j.apsusc.2015.05.055.
41 Y. Du, X. Xu, Q. Liu, L. Bai, K. Hang and D. Wang, *Sci. Total Environ.*, 2022, **806**, 150691, DOI: 10.1016/j.scitotenv.2021.150691.
42 M. H. Saleem, M. F. B. Mfarrej, K. A. Khan and S. A. Alharthy, *Sci. Total Environ.*, 2024, **913**, 169755, DOI: 10.1016/j.scitotenv.2023.169755.
43 M. Ahmed, M. O. Mavukkandy, A. Giwa, M. Elektorowicz, E. Katsou, O. Khelifi, V. Naddeo and S. W. Hasan, *npj Clean Water*, 2022, **5**, 12, DOI: 10.1038/s41545-022-00154-5.
44 G. Li, C. Yang, Q. He and J. Liu, *J. Environ. Chem. Eng.*, 2022, **10**, 107374, DOI: 10.1016/j.jece.2022.107374.
45 A. Gellé, T. Jin, L. de la Garza, G. D. Price, L. V. Besteiro and A. Moores, *Chem. Rev.*, 2020, **120**, 986, DOI: 10.1021/acs.chemrev.9b00187.
46 R. A. de Jesus, G. C. de Assis, R. J. de Oliveira, J. A. S. Costa, C. M. P. da Silva, M. Bilal, H. M. N. Iqbal, L. F. R. Ferreira and R. T. Figueiredo, *Environ. Technol. Innov.*, 2021, **24**, 101851, DOI: 10.1016/j.eti.2021.101851.
47 D. Zamel, A. U. Khan, A. Waris, A. Ebrahim and N. E. A. A. El-Sattar, *Results Chem.*, 2023, **6**, 101092, DOI: 10.1016/j.rechem.2023.101092.
48 S. A. Khan, M. Jain, A. Pandey, K. K. Pant, Z. M. Ziora, M. A. T. Blaskovich, N. P. Shetti and T. M. Aminabhavi, *J. Environ. Manage.*, 2022, **319**, 15675, DOI: 10.1016/j.jenvman.2022.115675.
49 S. Marimuthu, A. J. Antonisamy, S. Malayandi, K. Rajendran, P. C. Tsai, A. Pugazhendhi and V. K. Ponnusamy, *J. Photochem. Photobiol., B*, 2020, **205**, 111823, DOI: 10.1016/j.jphotobiol.2020.111823.
50 D. Garibo, H. A. Borbón-Nuñez and J. N. D. de León, *Sci. Rep.*, 2020, **10**, 12805, DOI: 10.1038/s41598-020-69606-7.
51 E. Z. Okka, T. Tongur, T. T. Aytas, M. Yilmaz, Ö. Topel and R. Sahin, *Optik*, 2023, **294**, 171487, DOI: 10.1016/j.ijleo.2023.171487.
52 H. Sulistyarti, M. M. Utama and A. M. Fadhila, *Anal. Sci.*, 2023, **39**, 335–346, DOI: 10.1007/s44211-022-00237-w.
53 B. Singh, A. Dhiman and S. Kumar, *Res. Surf. Interfaces*, 2024, **16**, 100256, DOI: 10.1016/j.rsurfi.2024.100256.
54 S. Song, Y. Zhao, X. Yuan and J. Zhang, *Colloids Surf. A*, 2019, **574**, 36, DOI: 10.1016/j.colsurfa.2019.04.047.
55 V. A. Sakkas, M. A. Islam, C. Stalikas and T. A. Albanis, *J. Hazard. Mater.*, 2010, **175**, 33–44, DOI: 10.1016/j.jhazmat.2009.10.050.
56 M. Harja, G. Buema and D. Bucur, *Sci. Rep.*, 2022, **12**, 6087, DOI: 10.1038/s41598-022-10093-3.
57 D. Gola, A. Kriti, N. Bhatt, M. Bajpai, A. Singh, A. Arya, N. Chauhan, S. K. Srivastava, P. K. Tyagi and Y. Agrawal, *Curr. Res. Green Sustain. Chem.*, 2021, **4**, 100132, DOI: 10.1016/j.crgsc.2021.100132.
58 A. Nyabadza, M. Makhesana, A. Plouze, A. Kumar, I. Ramirez, S. Krishnamurthy, M. Vazquez and D. Brabazon, *J. Environ. Chem. Eng.*, 2024, **12**, 112643, DOI: 10.1016/j.jece.2024.112643.
59 A. Bhankhar, M. Giri, K. Yadav and N. Jaggi, *Indian J. Phys.*, 2014, **88**, 1191, DOI: 10.1007/s12648-014-0555-x.
60 X. Liu, M. Liang and M. Liu, *Nanoscale Res. Lett.*, 2016, **11**, 440, DOI: 10.1186/s11671-016-1647-7.
61 M. Arif, F. Tahir, U. Fatima, R. Begum, Z. H. Farooqi, M. Shahid, T. Ahmad, M. Faizan, K. Naseem and Z. Ali, *Mater. Today Commun.*, 2022, **33**, 104700, DOI: 10.1016/j.mtcomm.2022.104700.
62 S. Iqbal, C. Zahoor, S. Musaddiq, M. Hussain, R. Begum, A. Irfan, M. Azam and Z. H. Farooqi, *Ecotoxicol. Environ. Saf.*, 2020, **202**, 110924, DOI: 10.1016/j.ecoenv.2020.110924.